Modeling of second-harmonic scanning optical microscopy of molecular quasi-one-dimensional aggregates

Valeri Z. Lozovski,[1] Jonas Beermann,[2] and Sergey I. Bozhevolnyi[2]
[1]*Department of Semiconductor Electronics, Radiophysical Faculty, National T. Shevchenko University, Glushkov avenue 2, Building 5, Kyiv UKR-03028, Ukraine*
[2]*Department of Physics and Nanotechnology, Aalborg University, Skjernvej 4A, DK-9220 Aalborg Øst, Denmark*
(Received 17 May 2006; revised manuscript received 8 November 2006; published 31 January 2007)

Far- and near-field second-harmonic scanning optical microscopy (SOM) of molecular quasi-one-dimensional aggregates, such as molecular nanoneedles, is modeled in the frame of the effective susceptibility concept formulated beyond the near-field approximation. Far- and near-field SOM images of molecular nanoneedles are calculated at both fundamental and second-harmonic frequencies for different polarization combinations. Far-field two-photon luminescence SOM is also considered, and the simulated images are found qualitatively consistent with the available experimental results.

DOI: 10.1103/PhysRevB.75.045438 PACS number(s): 42.30.Va, 07.79.Fc, 42.65.Ky, 07.60.Pb

I. INTRODUCTION

Intensive studies of organic molecules and their nanoaggregates as basic elements for future optoelectronic and electronic devices have been carried out utilizing different methods for adequate characterization of their properties.[1–3] Among these methods optical investigations are prevalent due to their versatility, noninvasiveness, spectral selectivity, and self-descriptiveness. Organic molecules can often be highly polarizable and assemble at the surface of a solid into large ordered noncentrosymmetric aggregates. In particular, the molecules can stack, producing quasi-one-dimensional forms. As a result, structures consisting of nanoneedles achieving hundreds of nanometers in length can be formed at the surface of a solid.[4,5] For example, the chemical formulas and structural forms of nanoaggregates of *para*-hexaphenylene[6] and metal-substituted phthalocyanine[7] are shown in Fig. 1. Considering the interaction of molecular aggregates with optical radiation, the knowledge of local-field distributions becomes very important for their investigation, because the local field at the molecules determines their optical and electrical characteristics.[8–10] In this connection, scanning optical microscopy (SOM), especially near-field SOM, is a convenient instrument for visualization of local-field distributions at molecular structures such as nanoneedles.[11–13] Organic molecular aggregates are often characterized by strong nonlinearities,[14–16] which can be probed and studied using nonlinear optical processes, e.g., second-harmonic generation. In particular, SOM at the second harmonic (SH) frequency can be successfully used for investigations of the properties of molecular systems.[17,18] The first experiments with near-field SH SOM (Refs. 19–21) demonstrated the efficiency of this technique for the visualization of local-field distributions and gave rise to intensive studies of different objects with SH scanning near-field optical microscopy (SNOM).[22–25] Subsequent advances in SH SOM experimental techniques[14–16] required the development of adequate theoretical modeling tools for simulation and interpretation of the SH SOM images. Thus, the standard method of solving the Lippmann-Schwinger equation to find the self-consistent fields based on a discretization scheme was first used.[26,27] Another approach is based on the effective susceptibility concept, which allows one to obtain an analytical solution of the Lippmann-Schwinger equation.[28–31] It is important to note that, in later studies,[28–33] the procedure of self-consistency for fields at both the fundamental harmonic (FH)

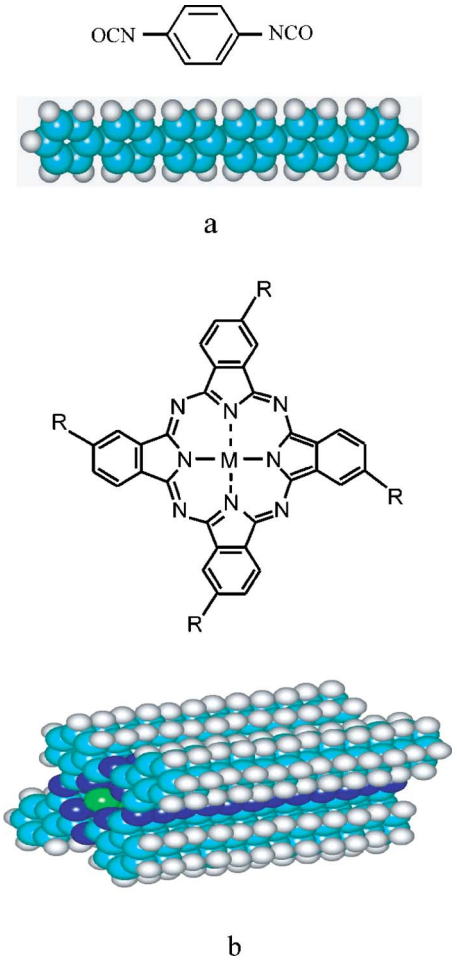

FIG. 1. (Color online) The chemical formulas and structural forms of organic molecular aggregates of *para*-hexaphenylene (a) and metal-substituted phthalocyanine (b).

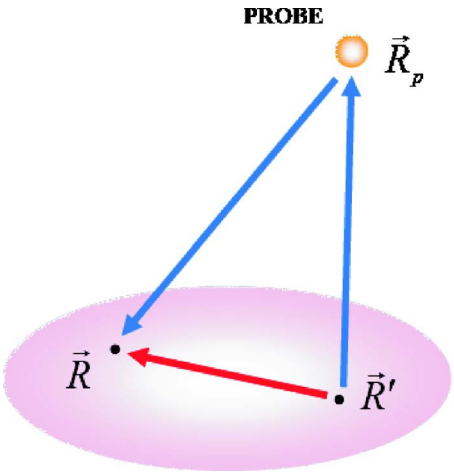

FIG. 2. (Color online) Sketch of light scattering processes in the object-probe system.

and SH frequencies was implemented. All these methods invoke the near-field approximation, and, strictly speaking, are applicable only for microscopy of objects whose linear dimensions are (much) smaller than the pump (FH) light wavelength. In order to model the SOM of objects whose linear dimensions are larger than the wavelength the above mentioned methods have to be reformulated.

In this work we report on modeling of both SH SNOM and SH scanning far-field optical microscopy (SFOM) of molecular quasi-one-dimensional aggregates, i.e., nanoneedles, based on the approach developed in our previous work.[28–31] In order to extend our approach beyond the near-field approximation, we use a series expansion for the photon propagator, including both near-, middle-, and far-field terms.

II. GENERAL SELF-CONSISTENT EQUATIONS

The general framework for modeling of the SH near- and far-field imaging used in this work was developed previously.[28–31] The main problem in modeling of SOM consists in taking into account nonlocal retarding interactions between different parts of an object, e.g., a nanoneedle in our case. This means that the Lippmann-Schwinger integral equation

$$E_i(\vec{R},\omega) = E_i^{(I)}(\vec{R},\omega) - i\omega\mu_0 \int_V d\vec{R}' G_{ij}(\vec{R},\vec{R}',\omega)\chi_{jl}(\omega)E_l(\vec{R}',\omega), \quad (1)$$

where ω is the FH frequency, should be solved using the Green's function $G_{il}(\vec{R},\vec{R}',\omega)$ with retardation being taken into account, i.e., beyond the near-field approximation. It has been shown[28–31] that the solution of Eq. (1) can be written via the effective susceptibility tensor

$$X_{ij}(\vec{R},\omega) = \{[\chi_{ij}(\omega)]^{-1} + S_{ji}(\vec{R},\omega)\}^{-1} \quad (2)$$

in the form

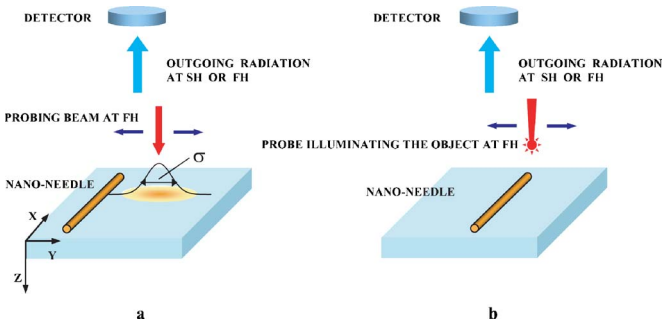

FIG. 3. (Color online) Schematics of the SOM systems under consideration: Scanning far-field optical microscopy (a) and scanning near-field optical microscopy (b).

$$E_i(\vec{R},\omega) = E_i^{(I)}(\vec{R},\omega) - i\omega\mu_0 \int_V d\vec{R}' G_{ij}(\vec{R},\vec{R}',\omega) \times X_{jl}(\vec{R}',\omega)E_l^{(I)}(\vec{R}',\omega), \quad (3)$$

where $\chi_{ij}(\omega)$ is the susceptibility tensor (describing the linear response on the local field) that characterizes the object material and V is the object (nanoneedle) volume, and $E_i^{(I)}(\vec{R},\omega)$ is the incident field which illuminates the object-substrate system. The self-energy part $S_{ji}(\vec{R},\omega)$ can be represented in the form

$$S_{ji}(\vec{R},\omega) = i\omega\mu_0 \int_V d\vec{R}' G_{ji}(\vec{R},\vec{R}',\omega). \quad (4)$$

The illuminating field is connected with a long-range external (incident from outside) field $E_j^{(0)}(\vec{R},\omega)$ by the relation

$$E_i^{(I)}(\vec{R},\omega) = I_{ij}(\vec{R},\omega)E_j^{(0)}(\vec{R},\omega), \quad (5)$$

where $I_{ij}(\vec{R},\omega)$ is the illumination tensor. In the case of SNOM, where illumination of the object is realized by a probe having coordinates $\vec{R}_p$, the illumination tensor can be presented in the form

$$I_{ij}(\vec{R},\omega) = -i\omega\mu_0 V_p \chi_p(\omega) G_{ij}^{(0)}(\vec{R},\vec{R}_p,\omega), \quad (6)$$

with V_p and $\chi_p(\omega)$ being the volume and electric susceptibility of the probe, respectively. In the case of SFOM using a Gaussian beam illumination, the illumination tensor is written in the form

$$I_{ij}(\vec{R}) = \exp\left(-\frac{(x-x_c)^2+(y-y_c)^2}{\sigma_0^2}\right)U_{ij}, \quad (7)$$

where U_{ij} is the unit tensor, x_c and y_c are the coordinates of the illumination spot center in the plane of the substrate surface, and σ_0 is the characteristic diameter of the light spot.

It should be mentioned that the Green's function in the case of SNOM has to be written in the form[29]

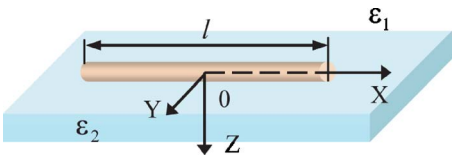

FIG. 4. (Color online) Scheme of the nanoneedle considered in the calculation.

$$G_{ij}(\vec{R},\vec{R}',\omega) = G_{ij}^{(0)}(\vec{R},\vec{R}',\omega) - i\omega\mu_0 V_p \chi_p(\omega) \times G_{il}^{(0)}(\vec{R},\vec{R}_p,\omega) G_{lj}^{(0)}(\vec{R}_p,\vec{R}',\omega), \quad (8)$$

which allows us to take into account the multiple scattering processes inside the probe-object-surface (of the substrate) system. Indeed, the first term of Eq. (8) describes the direct light propagation from point $\vec{R}'$ to point $\vec{R}$, but the second term of Eq. (8) describes the light propagation from point $\vec{R}'$ to point $\vec{R}$ via reradiation by the probe localized at point $\vec{R}_p$ (see Fig. 2). In the case of Gaussian beam illumination one should use the pseudovacuum Green's function $G_{ij}^{(0)}(\vec{R},\vec{R}',\omega)$,[11] which characterizes the electrodynamical properties of the substrate and surrounding medium (without the object).

As a result, the self-consistent FH field inside the object, in both schemes of illumination (with the probe or the Gaussian beam), can be represented in the general form

$$E_i(\vec{R},\omega) = L_{ij}(\vec{R},\omega) E_j^{(0)}(\vec{R},\omega), \quad (9)$$

with the local-field factor given by

$$L_{ij}(\vec{R},\omega) = I_{ij}(\vec{R},\omega) - i\omega\mu_0 \int_V d\vec{R}' G_{ik}(\vec{R},\vec{R}',\omega) X_{kl}(\vec{R}',\omega) I_{lj}(\vec{R}',\omega). \quad (10)$$

The knowledge of the self-consistent FH field is the first step toward determination of the self-consistent SH field. The main idea when finding the SH field is based on representing the effective SH current density inside the object as a sum of two parts[29]

$$J_i(\vec{R},2\omega) = J_i^{(L)}(\vec{R},2\omega) + J_i^{(N-L)}(\vec{R},2\omega), \quad (11)$$

where the linear contribution $J_i^{(L)}(\vec{R},2\omega)$ to the SH current density is driven by the self-consistent SH field, and the nonlinear contribution $J_i^{(N-L)}(\vec{R},2\omega)$ is induced (via SH generation) by the self-consistent FH field. These two contributions can be then expressed as follows:

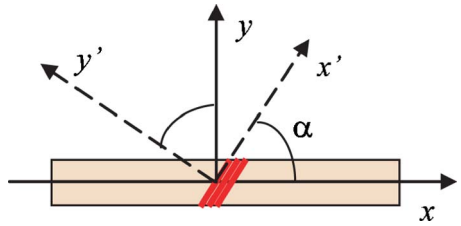

FIG. 5. (Color online) Laboratory (needle) and molecular coordinate frames.

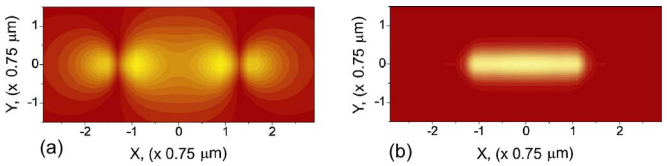

FIG. 6. (Color online) Near-field images of the short (1.8 μm) needle calculated at the FH (a) and SH (b) frequencies for xx polarization and depicted in units of the FH wavelength used (750 nm).

$$J_i^{(L)}(\vec{R},2\omega) = \chi_{ij}(2\omega) E_j(\vec{R},2\omega) \quad (12)$$

and

$$J_i^{(N-L)}(\vec{R},2\omega) = \chi_{ijk}^{(2)}(\omega,\omega;2\omega) E_j(\vec{R},\omega) E_k(\vec{R},\omega). \quad (13)$$

Applying the general framework developed previously,[29–31] one obtains for the self-consistent SH field

$$E_i(\vec{R},2\omega) = L_{ilk}^{(SH)}(\vec{R},\omega,\omega;2\omega) E_l^{(0)}(\vec{R},\omega) E_k^{(0)}(\vec{R},\omega), \quad (14)$$

where the SH local-field factor is given by

$$L_{ijk}^{(SH)}(\vec{R},2\omega) = I_{ijk}^{(SH)}(\vec{R},2\omega) - i2\omega\mu_0 \int_V d\vec{R}' G_{im}(\vec{R},\vec{R}',2\omega) \times X_{ml}(\vec{R}',2\omega) I_{ljk}^{(SH)}(\vec{R}',2\omega), \quad (15)$$

with the effective susceptibility [Eq. (2)] calculated at the SH frequency. The illumination tensor $I_{ijk}^{(SH)}(\vec{R},2\omega)$ connects the external field and incoming SH field

$$E_i^{(incoming)}(\vec{R},2\omega) = I_{ijk}^{(SH)}(\vec{R},2\omega) E_j^{(0)}(\vec{R},\omega) E_k^{(0)}(\vec{R},\omega), \quad (16)$$

and is given by

$$I_{ijk}^{(SH)}(\vec{R},2\omega) = -i2\omega\mu_0 \int_V d\vec{R}' G_{im}(\vec{R},\vec{R}',2\omega) \times \chi_{mng}^{(2)}(\omega,\omega;2\omega) L_{nj}(\vec{R},\omega) L_{gk}(\vec{R}',\omega), \quad (17)$$

where $\chi_{ijk}^{(2)}(\omega,\omega;2\omega)$ is the local nonlinear (second-order) susceptibility tensor.

Indeed, substituting Eqs. (12) and (13) in the equation for the self-consistent SH field, one obtains

$$E_i(\vec{R},2\omega) = E_i^{(incoming)}(\vec{R},2\omega) - i2\omega\mu_0 \int_V d\vec{R}' G_{ij}(\vec{R},\vec{R}',2\omega) \chi_{jl}(2\omega) E_l(\vec{R}',2\omega), \quad (18)$$

where the incoming SH field is

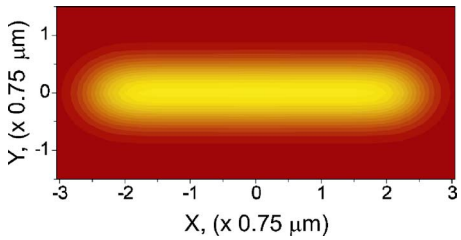

FIG. 7. (Color online) Far-field SH image of a single 3.6-μm-long nanoneedle calculated for xx polarization.

$$E_i^{(incoming)}(\vec{R},2\omega) = -i2\omega\mu_0 \int_V d\vec{R}' G_{im}(\vec{R},\vec{R}',2\omega) \times \chi^{(2)}_{mjl}(\omega,\omega;2\omega) E_j(\vec{R}',\omega) E_l(\vec{R}',\omega). \tag{19}$$

Once the self-consistent FH field is determined [via Eq. (9)] the incoming field in Eq. (18) becomes known and can thus be used for solving the problem of self-consistency at the SH frequency.

III. IMAGE FORMATION IN FAR- AND NEAR-FIELD MICROSCOPY

In this work we consider, for simplicity, the experimental setup typical for SOM operating in reflection mode (Fig. 3). Let us assume that the external field $\vec{E}^{(0)}$ is linearly polarized along either the x or y axis. To obtain expressions for the field intensity being recorded with a detector (as a function of the scanning coordinates), we separately consider the two cases of the detected signal being at the FH and SH frequency, respectively.

A. Imaging at the fundamental harmonic frequency

A scanning probe (Gaussian beam), which is moved along the plane parallel to a substrate surface, induces currents at the FH frequency inside the object and substrate. These currents (connected with the local field via the constitutive equation) create the FH field $E_i^{FF}(\vec{R}_d,\omega)$ at the (remote) detector situated in the far-field (FF) zone:

$$E_i^{FF}(\vec{R}_d,\omega) = -i\omega\mu_0 \int_V d\vec{R}' G_{im}(\vec{R}_d,\vec{R}',\omega) \chi_{mn}(\vec{R}',\omega) E_n(\vec{R}',\omega). \tag{20}$$

The dependence of the FH field intensity at the detector on the scanning coordinates forms the near- or far-field image of the object (nanoneedle). Let us take into account that the distance between the object and detector $|\vec{R}_d - \vec{R}_{obj}|$ is considerably larger than the linear dimensions of the object. Then, in the coordinate system having the origin coinciding with the nanoneedle center, one can use the following approximation for all $\vec{R}' \in V$: $G_{ij}(\vec{R}_d,\vec{R}',\omega) \approx G_{ij}(\vec{R}_d - \vec{R}_{obj},\omega)$ $\approx G_{ij}(\vec{R}_d,\omega)$. The FH field intensity at the detector $|E_i^{FF}(\vec{R}_d,\omega)|^2$ can then be written down as follows:

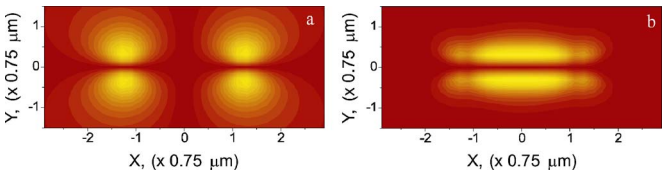

FIG. 8. (Color online) Near-field images of the short (1.8 μm) needle calculated at the FH (a) and SH (b) frequencies for xy polarization.

$$W(\vec{R}_d,\omega) = |G_{ii}^{(0)}(\vec{R}_d,\omega)|^2 \left| \omega\mu_0 \int_V d\vec{R}' \chi_{in}(\omega) L_{nj}(\vec{R}',\omega) \right|^2 \times |E_j^{(0)}(\omega)|^2. \tag{21}$$

The first factor on the right-hand side of Eq. (21) characterizes the experimental setup and plays the role of a setup function, which is constant during the scanning and can be considered as a normalizing factor. This implies that the FH images (obtained with SNOM or SFOM) can be described with the following expression keeping the essential terms of Eq. (21):

$$P_{ij}(\vec{R}_d,\omega) = \left| \omega\mu_0 \int_V d\vec{R}' \chi_{in}(\omega) L_{nj}(\vec{R}',\omega) \right|^2. \tag{22}$$

B. Imaging at the second-harmonic frequency

The scanning probe (Gaussian beam) induces currents inside the object and substrate at both FH and SH frequencies resulting in the self-consistent SH field $E_i(\vec{R},2\omega)$ [Eq. (14)], which can be related, in turn, to the self-consistent current at the SH frequency:

$$J_i^{(s-c)}(\vec{R},2\omega) = \chi_{ij}(\vec{R},2\omega) E_j(\vec{R},2\omega). \tag{23}$$

The SH field $E_i^{FF}(\vec{R}_d,2\omega)$ at the detector in the far-field zone induced by the above SH current can then be written in the form

$$E_i^{FF}(\vec{R}_d,2\omega) = -i2\omega\mu_0 \int_V d\vec{R}' G_{im}(\vec{R}_d,\vec{R}',2\omega) \times \chi_{mn}(2\omega) E_n(\vec{R}',2\omega). \tag{24}$$

Taking again into account that the distance between the scanning area and the detector is much larger than the object's linear dimensions, one can (analogously to the previous case) reduce the expression for the SH field intensity at the detector [Eq. (24)] to the following form:

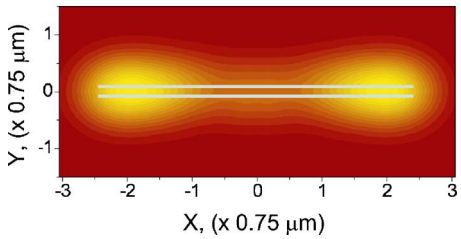

FIG. 9. (Color online) Far-field SH image of two parallel long nanoneedles separated by a distance of 0.18 μm (schematically shown as gray lines) and calculated for *xx* poloarization.

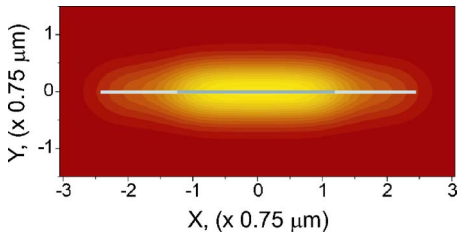

FIG. 10. (Color online) Far-field SH image of inhomogeneous long nanoneedle calculated for *xx* polarization. The region of high values of susceptibilities is schematically shown as dark gray.

$$W(\vec{R}_d,2\omega) = |G_{it}^{(0)}(\vec{R}_d,2\omega)|^2 \times \left| 2\omega\mu_0 \int_V d\vec{R}'\, \chi_{in}(2\omega) L_{njj}^{(SH)}(\vec{R},2\omega) \right|^2 |E_j^{(0)}(\omega)|^4. \tag{25}$$

Note that, within these approximations, nondiagonal components of the Green's dyadic being negligibly small in comparison with the diagonal ones are omitted. As a result, one can conclude that the SH image, i.e., the dependence of the SH field intensity $W(\vec{R}_d,2\omega)/|E_j^{(0)}(\omega)|^4$ at the detector as a function of the scanning probe (or a center of the Gaussian beam) coordinates is determined by the expression

$$N_{ij}(\vec{R}_d,2\omega) = \left| 2\omega\mu_0 \int_V d\vec{R}'\, \chi_{in}(2\omega) L_{njj}^{(SH)}(\vec{R},2\omega) \right|^2. \tag{26}$$

The tensor structure of N_{ij} and P_{ij} has a clear physical meaning, viz., the value of the corresponding tensor component is proportional to the intensity of the local-field component polarized along the i axis and with the external field polarized along the j axis.

Finally, we would like to remark that, while the value of N_{ij} determines the near- or far-field SH image, the near- or far-field images in the case of two-photon-absorption-induced luminescence are determined by the value of P_{ij}. Indeed, the process of two-photon luminescence (TPL) consists of two stages. The first stage is the absorption of two photons of frequency ω by the system. The second stage is the transition of the excited system to the ground state with emission of a photon (of frequency $\Omega > \omega$). The process of two-photon absorption is defined by the square of the local-field intensity.[34–36] The intensity of TPL is thereby proportional to the local-field intensity squared, implying that the TPL images are proportional to the value of $P_{ij}(\vec{R}_d,\omega)^2$. The calculation of the spatial distributions of P_{ij} and N_{ij} is the main task of the present consideration.

IV. NUMERICAL CALCULATIONS

In order to explore the main features of SOM of nanoneedles, we consider hypothetical quasi-one-dimensional molecular aggregates, choosing the parameters that would allow us to clearly see the characteristic traits of SNOM and SFOM images of nanoneedles and, at the same time, to compare the calculated images with those obtained experimentally. Consequently, we have chosen sufficiently large values of nonlinear susceptibilities of the molecular aggregates, assuming that only three susceptibility components play an essential role in forming the response from the molecular aggregates at the SH frequency. The numerical calculations were carried out with the following system parameters (Fig. 4). The nanoneedles were considered to be shaped as elliptical cylinders with half-axes $r_\parallel = 18$ nm (parallel to the substrate surface) and $r_\perp = 1.8$ nm (perpendicular to the surface). Two kinds of needles were considered; a short needle with the length $l = 1.8$ μm and a long needle with the length $l = 3.6$ μm. It has been supposed that the nanoneedles were formed as sets of molecular sticks whose main axis is rotated by an angle $\alpha = 72°$ relative to the main axis of the nanoneedle[37,38] as shown in Fig. 5. Because organic molecules interacting with the surface of a solid are often strongly polarized, one should take into account that the polarizability component normal to the surface will differ from its lateral components (even for spherically symmetric molecules). On the other hand, the nanoneedle represents a monoaxial structure. Under these circumstances, we considered that the linear susceptibility tensor of the nanoneedles has the following components: $\chi_{xx} = 0.71$, $\chi_{yy} = 0.18$, $\chi_{zz} = 0.2$. As mentioned above, it was assumed that the nanoneedles are formed by molecular sticks with relatively large nonlinearity so that the corresponding nonlinear susceptibility tensor has only three nonzero components: $\chi^{(2)}_{x'x'x'} = 0.001$ and $\chi^{(2)}_{y'x'x'} = \chi^{(2)}_{z'x'x'} = 0.0005$ (given in arbitrary units). Here, the coordinate axis x' is directed along the long molecular axes, and the axes y' and z' are located in the plane perpendicular to the x' axis so that the z' axis is perpendicular to the substrate surface. Bearing in mind that the molecules are oriented with their long axes at the angle $\alpha = 72°$ with the nanoneedle axis (see Fig. 5), one should use the usual expressions $\chi_{ij} = c_{ii'} c_{jj'} \chi_{i'j'}$ and $\chi^{(2)}_{ijk} = c_{ii'} c_{jj'} c_{kk'} \chi^{(2)}_{i'j'k'}$ ($c_{jj'}$ is the cosine of the angle between the j axis in the laboratory and the j' axis in the molecular coordinate system), which relate the susceptibility tensor components of the nanoneedles in the molecule coordinate system to those in the laboratory coordinate system. As a result, both linear and nonlinear susceptibility tensors become rather complicated; namely, there are five nonzero and different components of the linear susceptibility tensor, χ_{xx}, χ_{xy}, χ_{yx}, χ_{yy}, and χ_{zz}, and 12 nonzero components of the nonlinear second order susceptibility tensor, $\chi^{(2)}_{xxx}$, $\chi^{(2)}_{xxy}$, $\chi^{(2)}_{xyx}$, $\chi^{(2)}_{xyy}$, $\chi^{(2)}_{yxx}$, $\chi^{(2)}_{yxy}$, $\chi^{(2)}_{yyx}$, $\chi^{(2)}_{yyy}$, $\chi^{(2)}_{zxx}$, $\chi^{(2)}_{zxy}$, $\chi^{(2)}_{zyx}$, and $\chi^{(2)}_{zyy}$.

In the case of SNOM imaging, we considered that the probe having a radius $r_p=15$ nm and electrical susceptibility $\chi_p=3.7$ was scanned along the plane $Z_p=325$ nm. In the case of SFOM imaging, the diameter of the Gaussian beam was chosen to be $\sigma=325$ nm. The FH wavelength of the incoming field was set to 750 nm. To correctly take the multiple scattering processes inside (rather long) nanoneedles into account, one has to go beyond the near-field approximation and employ the complete form of the Green's dyadic, viz.,

$$\overleftrightarrow{G}^{(0)}(\vec{R},\vec{R}',\omega)=\frac{1}{4\pi k_0^2}\left[\left(-\frac{1}{R}-\frac{ic}{\omega R^2}+\frac{c^2}{\omega^2 R^3}\right)\overleftrightarrow{U}+\left(\frac{1}{R}+i\frac{3c}{\omega R^2}-\frac{3c^2}{\omega^2 R^3}\right)\vec{e}_R\vec{e}_R\right]e^{i(\omega/c)R}, \tag{27}$$

including all terms. The real and imaginary parts of the near- and middle-field contributions to the Green's dyadic have the following form:

$$\mathrm{Re}\,\overleftrightarrow{G}^{(0)}_{NF+MF}(\vec{R},\vec{R}',\omega)=\frac{1}{4\pi k_0^2}\frac{-3\vec{R}\cdot\vec{R}+R^2\overleftrightarrow{U}}{R^3}\times\left(\frac{1}{(k_0R)^2}+\frac{1}{2}-\frac{1}{8}(k_0R)^2\right),$$

$$\mathrm{Im}\,\overleftrightarrow{G}^{(0)}_{NF+MF}(\vec{R},\vec{R}',\omega)=\frac{1}{4\pi k_0^2}\frac{-3\vec{R}\cdot\vec{R}+R^2\overleftrightarrow{U}}{R^3}\times\left(\frac{1}{3}(k_0R)-\frac{1}{24}(k_0R)^3\right), \tag{28}$$

with the corresponding parts of the far-field contribution being as follows:

$$\mathrm{Re}\,\overleftrightarrow{G}^{(0)}_{FF}(\vec{R},\vec{R}',\omega)=\frac{1}{4\pi k_0^2}\frac{\vec{R}\cdot\vec{R}-R^2\overleftrightarrow{U}}{R^3}\times\left(1-\frac{1}{2}(k_0R)^2+\frac{1}{24}(k_0R)^4\right),$$

$$\mathrm{Im}\,\overleftrightarrow{G}^{(0)}_{FF}(\vec{R},\vec{R}',\omega)=\frac{1}{4\pi k_0^2}\frac{\vec{R}\cdot\vec{R}-R^2\overleftrightarrow{U}}{R^3}\left((k_0R)-\frac{1}{6}(k_0R)^3\right), \tag{29}$$

with $R^2=(x-x')^2+(y-y')^2+(z-z')^2$ and $k_0=\omega/c$. It has been shown[39] that taking into account a linear substrate leads only to small rescaling of the SH near-field images. Therefore, for the sake of simplicity, we assumed in this work that the influence of a substrate on the formation of the local field can be described within the near-field approximation and used the indirect part of the Green's dyadic in the form

$$I_{ij}(\vec{R},\vec{R}',\omega)=-\Omega(\omega)\frac{1}{\tilde{R}^5}\begin{pmatrix}\tilde{R}^2-3(x-x')^2 & 3(x-x')(y-y') & 3(x-x')(z-z')\\ -3(x-x')(y-y') & \tilde{R}^2-3(y-y')^2 & 3(y-y')(z-z')\\ -3(x-x')(y-y') & -3(y-y')(z-z') & -\tilde{R}^2+3(z-z')^2\end{pmatrix}, \tag{30}$$

with

$$\Omega(\omega)=\frac{1}{4\pi k_0^2}\frac{\varepsilon_2(\omega)-1}{\varepsilon_2(\omega)+1} \tag{31}$$

and

$$\tilde{R}=\sqrt{(x-x')^2+(y-y')^2+(z+z')^2}, \tag{32}$$

where $\varepsilon_2(\omega)$ is the dielectric function of the substrate.

Many integrals that should be calculated in order to find the self-consistent field are improper due to singularity of the Green's dyadic function at $R=0$. This problem is well known and related to the radiation reaction of the field. The problem can be solved by making use of the concept of exclusion volume.[40,41] The main idea is to introduce the exclusion volume V_δ whose depolarizing properties are accounted for by a special source tensor. For example, when calculating the self-consistent field the following relation should be applied:

$$E_i(\vec{R})=-i\omega\mu_0\lim_{\delta\to 0}\int_{V-V_\delta}d\vec{R}'G_{il}(\vec{R},\vec{R}')J_l(\vec{R}')-\frac{1}{i\omega\mu_0}L_{il}J_l(\vec{R}), \tag{33}$$

where L_{il} is the source tensor, which depends solely on the geometry of the exclusion volume V_δ. For cylinder length l and radius r_n, L_{il} has three nonzero components

$$L_{xx}=1-\frac{l}{\sqrt{l^2+r_n^2}},\quad L_{yy}=L_{zz}=\frac{l}{2\sqrt{l^2+r_n^2}}. \tag{34}$$

One should note that, because the solutions of the near- and far-field image visualization problem at both FH and SH frequencies were obtained analytically, the numerical calculations were reduced to simple tabulation of the functions in the right parts of Eqs. (22) and (26). Consequently, only the problem of correct numerical calculations of the three-dimensional 3D integrals, as discussed above, was nontrivial.

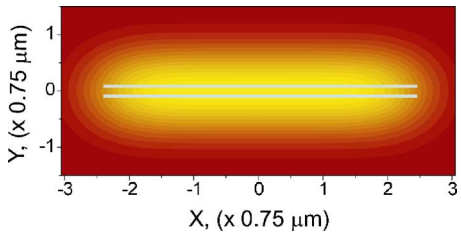

FIG. 11. (Color online) Far-field FH image of two parallel and long nanoneedles separated by a distance of 0.18 μm (schematically shown as gray lines) and calculated for *xx* polarization.

V. RESULTS AND DISCUSSION

The near- and far-field SOM images of molecular nanoneedles at both FH and SH frequencies were calculated for different polarization configurations. Here we use the following notation. *ij* polarization means that the external illuminating field is polarized along the *j* axis of the laboratory coordinate system, and the field detected in the far-field zone is polarized along the *i* axis. Aiming at a qualitative analysis of near- and far-field images of different configurations of the nanoneedles, we shall not compare the intensity values at the detector, but restrict ourselves to considering only the image appearances. As usual, the brightness in the presented images is proportional to the field intensity at the (remote) detector. The near-field FH and SH images calculated for the short (1.8 μm) needle are shown in Figs. 6 and 7 for the main polarization configurations.

The appearance of the FH near-field image calculated for a co-polarized configuration are rather anticipatory being very similar to previous FH images for the objects with simple shapes.[29,42] On the other hand, the SH near-field images demonstrate a strong localization of the SH field to the object. Similar results were obtained for other polarization configurations. As an example, Fig. 8 shows the near-field FH and SH images of a single short nanoneedle, calculated for a cross-polarized *xy* configuration. Note that the maxima of the local field intensity for both FH and SH images are located outside the object, but the SH local-field distribution has maximal values almost along the entire side of the nanoneedle. Obviously, this can be explained by a rather strong nonlinear polarization for this configuration, being supplied mainly by the $\chi^{(2)}_{xyy}$ component. It should be noted

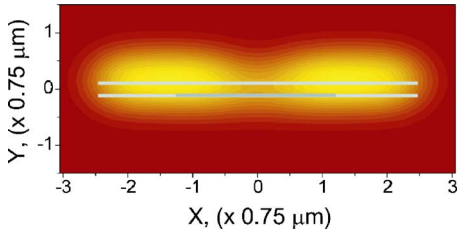

FIG. 12. (Color online) Far-field SH image calculated for *xx* polarization from a pair of parallel nanoneedles, of which one is inhomogeneous along its main axis. The separation between the nanoneedles is 0.18 μm as shown schematically by gray lines and with the domain having increased susceptibility values marked as dark gray.

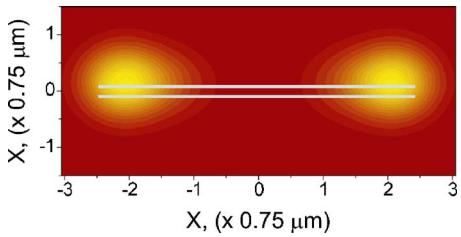

FIG. 13. (Color online) Far-field SH image of the two parallel long nanoneedles separated by a distance of 0.18 μm (schematically shown as gray lines) and calculated for *xy* polarization.

that, due to the complicated tensor structure of both the linear and nonlinear susceptibilities for the considered nanoneedles, one cannot make a simple analysis of the SH images based on symmetry aspects.

The far-field images were calculated for the long (3.6 μm) nanoneedles and the main results are shown in Figs. 8–13. As in the case of the near-field images (Figs. 6 and 7) the far-field SH image of a single nano-needle (Fig. 7) shows that the SH field is strongly localized at the object. The SH local field maximum appear as a homogeneous bright area, spread along the needle. It should be noted that, since the linear dimension of the molecular aggregates forming the nanoneedle is less than the wavelength, one can assume the needle to be a homogeneous structure. Despite the fact that in a real situation the nanoneedles of *para*-hexaphenylene aggregates are structures consisting of numerous molecular sticks, using this approximation qualitatively gives rather acceptable results close to those obtained experimentally.[38] However, these experiments also showed some variations of the nonlinear signal along the needles.[38] In order to explain such features, we calculated the far-field images from two parallel needles separated by a distance of 0.18 μm. The SH image of these needles, calculated for *xx*-polarization, is shown in Fig. 9. As seen, the interference between the local fields caused by each of the needles shifts the high field density to the ends of the needles. Another possible reason for variations in the SH intensity can be inhomogeneities of the needle along its main axis. To visualize such an effect, we calculated the far-field SH image from a 3.6-μm-long nanoneedle having a central piece (1.8 μm along the main axis) characterized by twice the usual susceptibility values (Fig. 10). As seen from Fig. 10, there is an area of increased SH intensity along the inhomogeneous nano-needle. It is interesting to note that the far-field FH image, calculated for the pair of nanoneedles, actually has the domain of strong field localization between the needles (see Fig. 11). The common influence of inhomogeneity and

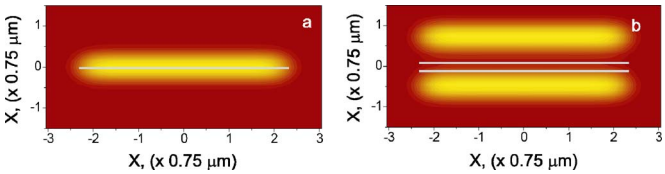

FIG. 14. (Color online) Far-field TPL images (4.65 $\times 2.25$ μm^2) of a single long nanoneedle (a) and of two nanoneedles (b) both calculated for *yy* polarization.

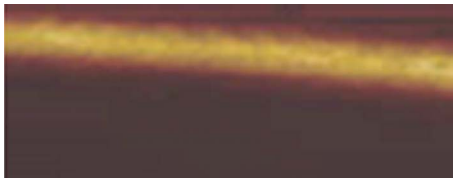

FIG. 15. (Color online) Experimental far-field TPL image (7.24×2.93 μm^2) of a single molecular *para*-hexaphenylene nanoaggregate obtained for *yy* polarization.

interaction between needles can lead to different appearance of the images. Figure 12 shows the far-field SH image from a pair of parallel nanoneedles, of which one is inhomogeneous along its main axis. The location of the inhomogeneous domain and the distance between the needles were chosen as in the previous case, but with a selected difference in susceptibility values along the inhomogeneous nanoneedle of only ~7%. As seen from Fig. 12, the domain of high SH intensity is located near the susceptibility jump. This means that the variations in the experimentally obtained SH intensity distribution along the nanoneedles can be explained by interference between the fields caused by different inhomogeneous nanoneedles situated closely to each other. A similar situation arises in the case of cross polarization. Figure 13 shows the far-field SH image from a pair of homogeneous nanoneedles calculated for *xy* polarization. The circumstance that the domains of strong local SH fields are shifted slightly toward one of the needles can probably be related to interference between the SH fields and strong anisotropy of the system under consideration. Indeed, the respective components of the nonlinear response tensor have the form $\chi_{xyy}=0.27\chi_{x'x'x'}-0.87\chi_{y'x'x'}$ and $\chi_{yxx}=0.09\chi_{x'x'x'}+0.03\chi_{y'x'x'}$. This means that the molecular aggregate responses to the *y* and *x* components of the incoming fields are very different. In the case under consideration, the interactions between nanoneedles, which are characterized by strong anisotropic nonlinear susceptibilities, apparently could lead to a nonsymmetric distribution of the local SH field. This fact could be considered as a reason for that uncommon view of the SH far-field image shown in Fig. 13. We would like to emphasize that, regardless of the fact that the needle diameter is much less than the needle length, the widths of the SH spot along the *x* and *y* axes are comparable. This can be explained by two reasons. The first of them is connected with the tensor structure of the nanoneedle, for which the $\chi^{(2)}_{yxx}$ component is comparable with the $\chi^{(2)}_{xxx}$ component. The second reason is the interference between self-consistent SH fields induced by SH currents in different parts inside the nanoneedle. Due to this interference, which is mainly realized via the environment, the area of strong SH field localization is appreciably large.

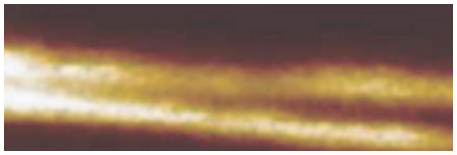

FIG. 16. (Color online) Experimental far-field TPL image (8.45×2.93 μm^2) of two molecular *para*-hexaphenylene nanoaggregates obtained for *yy* poloarization.

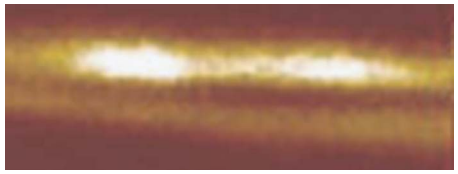

FIG. 17. (Color online) Experimental far-field TPL image (7.24×2.93 μm^2) of two molecular *para*-hexaphenylene nanoaggregates obtained for *xy* polarization.

The calculations of TPL were done for the long nanoneedles. Figure 14 shows the far-field TPL images calculated for one and two nanoneedles. Here we chose the Gaussian beam radius to be 0.2λ in order to have the relations between the needle width and wavelength of the scanning beam close to the experimental situation. Comparing the far-field TPL image from a single nanoneedle calculated for *yy* polarization [Fig. 14(a)] to the same obtained experimentally (see Fig. 15), there is an apparent qualitative agreement between these images. On the other hand, comparing the TPL images for two closely situated needles calculated here [Fig. 14(b)] and obtained experimentally (Fig. 16), one can see some differences. The main difference is the absence of bright spots in the calculated TPL image. The appearance of these spots in the experimental TPL images can be explained by several reasons. We think that the main reason is inhomogeneity of the needles. Indeed, calculations of the TPL image for a two needles where one of them has a domain characterized by ~6% higher susceptibility values produce results (not shown here) very close to the experimental ones (see Fig. 17). The increased TPL intensity from the left part of the needles in Fig. 16 can be explained by the slightly decreasing space between the needles causing stronger field interaction and local-field enhancement. Numerical calculations performed for such coupled nanoneedles situated close to each other give us similar results (not shown here). The cross polarized experimental TPL images were often characterized by bright spots along the nanoneedle area (Fig. 17). The numerical calculations for cross-polarized configurations produce similar results (Fig. 18). This suggest that, similar to the case of *yy* polarization, the far-field TPL images obtained for cross polarization are influenced both by interference of the local field related to coupled needles and by intrinsic properties of the formation of local fields.

In conclusion, the proposed approach for modeling near- and far-field scanning optical microscopy gives a qualita-

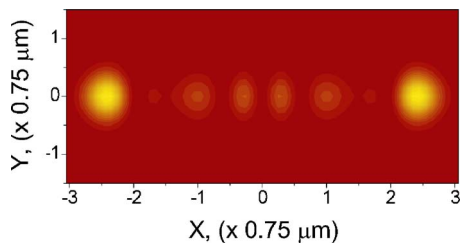

FIG. 18. (Color online) Far-field TPL image (4.65×2.25 μm^2) of a single long nanoneedle calculated for *xy* polarization.

tively good agreement with the experimentally obtained images of molecular nanoneedles. The approach is based on the effective susceptibility concept, which allows one to write the analytical solution for self-consistent fields at both fundamental- and second-harmonic frequencies. In addition, the TPL effects can be calculated in the frame of the developed approach. It should be noted that calculations of the SH field at the detector and the field caused by TPL processes are performed within different schemes: That is, the field radiated to the detector by TPL is calculated as a non-self-consistent field caused by the currents connected with the self-consistent FH field. On the other hand, the SH field detected in the far-field zone was calculated as a self-consistent field caused by both nonlinear and linear contributions of the currents. Moreover, the proposed approach in fact allows us to obtain the analytical solution of the self-consistent procedure and the numerical calculations were finally reduced to simple tabulation of the analytical formula. This circumstance leads to considerable reduction of computing time, which is an important feature of the approach. Moreover, because the method is based on the effective susceptibility concept, the main information about interactions inside the considered system is contained in the self-energy part. The approximations used during analytical estimations may have only quantitative and not qualitative influence on the results. This fact allows us to expect that the proposed approach could be useful for modeling near- and far-field images of rather complicated molecular or solid nanoneedles.

ACKNOWLEDGMENT

The authors acknowledge support from the NABIIT project (Contract No. 2106-05-0033 from the Danish Research Agency).

[1] W. E. Moerner and D. P. Fromm, Rev. Sci. Instrum. **74**, 3597 (2003).
[2] M. Muccini *et al.*, J. Opt. A, Pure Appl. Opt. **2**, 577 (2000).
[3] Z. P. Ou *et al.*, J. Porphyr. Phthalocyanines **9**, 398 (2005).
[4] M. Sayar and S. I. Stupp, Phys. Rev. E **72**, 011803 (2005).
[5] F. Sasaki, S. Hiraichi, and S. Kobayashi, IEEE J. Sel. Areas Commun. **23**, 1385 (2005).
[6] F. Balzer, V. G. Bordo, A. C. Simonsen, and H.-G. Rubahn, Phys. Rev. B **67**, 115408 (2003).
[7] R. A. Hann, S. K. Gupta, J. R. Fryer, and B. L. Eyers, Thin Solid Films **134**, 35 (1985).
[8] K. Kajikawa, T. Iososhima, H. Sasabe, W. Knoll, T. Yamada, and H. Takezoe, Mol. Cryst. Liq. Cryst. Sci. Technol., Sect. B: Nonlinear Opt. **15**, 127 (1996).
[9] F. C. Spano and S. Mukamel, Phys. Rev. A **40**, 5783 (1989).
[10] H. M. Abdel-Halim, J. Chem. Phys. **119**, 484 (2003).
[11] O. Keller, Phys. Rep. **268**, 85 (1996).
[12] Ch. Girard, Ch. Joachim, and S. Gauthier, Rep. Prog. Phys. **63**, 893 (2000).
[13] I. Young, IEEE Eng. Med. Biol. Mag. **15**, 59 (1996).
[14] G. J. Ashwell, J. Ewington, and K. Moczko, J. Mater. Chem. **15**, 1154 (2005).
[15] E. Gubbelmans *et al.*, Polymer **46**, 1784 (2005).
[16] F. Balzer, K. A. Shamery, R. Neuendorf, and H.-G. Rubahn, Chem. Phys. Lett. **368**, 307 (2003).
[17] P. J. Campagnola and L. M. Loew, Nat. Biotechnol. **21**, 1356 (2003).
[18] O. Slyadneva, A. Harata, and Y. Hatano, Anal. Sci. **17**, suppl. i1173 (2001).
[19] I. I. Smolyaninov, A. Zayats, and Ch. Davis, in *Proceedings of the 10th IEEE Laser, Electronics and Optical Society Annual Meeting*, LEOS, 1997 (unpublished), Vol. 2, pp. 182–183.
[20] I. I. Smolyaninov, A. V. Zayats, and C. C. Davis, Phys. Rev. B **56**, 9290 (1997).
[21] S. I. Bozhevolnyi and K. Pedersen, Surf. Sci. **377-379**, 384 (1997).
[22] I. I. Smolyaninov, C. H. Lee, and C. C. Davis, Tech. Dig. Ser.-Opt. Soc. Am. **7**, 228 (1998).
[23] S. I. Bozhevolnyi, K. Pedersen, T. Skettrup, X. Zhang, and M. Belmonte, Opt. Commun. **152**, 221 (1998).
[24] S. I. Bozhevolnyi and T. Geisler, J. Opt. Soc. Am. A **15**, 2156 (1998).
[25] M. Adameck, R. Blum, and M. Eich, Appl. Phys. Lett. **73**, 2884 (1998).
[26] A. Liu and G. W. Bryant, Phys. Rev. B **59**, 2245 (1999).
[27] G. W. Bryant and A. Liu, Superlattices Microstruct. **25**, 361 (1999).
[28] S. I. Bozhevolnyi, V. Z. Lozovski, K. Pedersen, and J. M. Hvam, Phys. Status Solidi A **175**, 331 (1999).
[29] S. I. Bozhevolnyi and V. Z. Lozovski, Phys. Rev. B **61**, 11139 (2000).
[30] S. I. Bozhevolnyi and V. Z. Lozovski, Phys. Rev. B **65**, 235420 (2002).
[31] S. I. Bozhevolnyi and V. Z. Lozovski, Physica E (Amsterdam) **15**, 229 (2002).
[32] Z. Y. Li, B. Y. Gu, and G. Z. Yang, Phys. Rev. B **59**, 12622 (1999).
[33] A. F. Xie, B. Y. Gu, G. Z. Yang, and Z. B. Zhang, Phys. Rev. B **63**, 054104 (2001).
[34] B. Ya. Zeldovich and T. I. Kuznetsova, Usp. Fiz. Nauk **106**, 47 (1972).
[35] V. M. Griban, O. V. Melnichuk, L. M. Ovander, and E. F. Venger, Semicond. Phys., Quantum Electron. Optoelectron. **3**, 144 (2000).
[36] A. M. Glass, A. Wokaun, J. P. Heritage, J. G. Berman, P. F. Liao, and D. H. Olson, Phys. Rev. B **24**, 4906 (1981).
[37] F. Balzer and H.-G. Rubahn, Adv. Funct. Mater. **15**, 17 (2005).
[38] J. Beermann, S. I. Bozhevolnyi, V. G. Bordo, and H.-G. Rubahn, Opt. Commun. **237**, 423 (2004).
[39] S. I. Bozhevolnyi, V. Z. Lozovski, and Yu. Nazarok, Opt. Spectrosc. **90**, 416 (2001).
[40] J. van Bladel, *Singular Electromagnetic Fields and Sources* (Clarendon, Oxford, 1991).
[41] A. D. Yaghjian, Proc. IEEE **68**, 248 (1980).
[42] O. J. F. Martin, C. Girard, and A. Dereux, J. Opt. Soc. Am. A **31**, 1801 (1996).